

Submillimeter arcsecond-resolution mapping of the highly collimated protostellar jet HH 211

Chin-Fei Lee^{1,2}, Paul T.P. Ho^{1,3}, Aina Palau⁴, Naomi Hirano¹, Tyler L. Bourke³, Hsien Shang¹, and Qizhou Zhang³

ABSTRACT

We have mapped the protostellar jet HH 211 in 342 GHz continuum, SiO ($J = 8 - 7$), and CO ($J = 3 - 2$) emission at $\sim 1''$ resolution with the Submillimeter Array (SMA). Thermal dust emission is seen in continuum at the center of the jet, tracing an envelope and a possible optically thick compact disk (with a size < 130 AU) around the protostar. A knotty jet is seen in CO and SiO as in H_2 , but extending closer to the protostar. It consists of a chain of knots on each side of the protostar, with an interknot spacing of $\sim 2''-3''$ or 600–900 AU and the innermost pair of knots at only $\sim 1.7''$ or 535 AU from the protostar. These knots likely trace unresolved internal (bow) shocks (i.e., working surfaces) in the jet, with a velocity range up to ~ 25 km s⁻¹. The two-sided mass-loss rate of the jet is estimated to be $\sim (0.7 - 2.8) \times 10^{-6} M_{\odot} \text{ yr}^{-1}$. The jet is episodic, precessing, and bending. A velocity gradient is seen consistently across two bright SiO knots (BK3 and RK2) perpendicular to the jet axis, with $\sim 1.5 \pm 0.8$ km s⁻¹ at $\sim 30 \pm 15$ AU, suggesting a presence of a jet rotation. The launching radius of the jet, derived from the potential jet rotation, is $\sim 0.15-0.06$ AU in the inner disk.

Subject headings: stars: formation — ISM: individual: HH 211 — ISM: jets and outflows.

¹Academia Sinica Institute of Astronomy and Astrophysics, P.O. Box 23-141, Taipei 106, Taiwan; cflee@asiaa.sinica.edu.tw

²Harvard-Smithsonian Center for Astrophysics, Submillimeter Array, 645 North A'ohoku, Hilo, HI 96720

³Harvard-Smithsonian Center for Astrophysics, 60 Garden Street, Cambridge, MA 02138

⁴Laboratorio de Astrofísica Espacial y Física Fundamental, INTA, Apartado 50727, E-28080 Madrid, Spain

1. Introduction

Protostellar jets are seen associated with low-mass protostars in the early stages of star formation. In spite of numerous studies, their physical properties (e.g., speed, episodic nature, collimation, and angular momentum) and thus launching mechanisms are still not well understood. They are believed to be launched from accretion disks around the protostars (see recent reviews by e.g., Pudritz et al. 2007; Ray et al. 2007; Shang et al. 2007), allowing us to probe the accretion process, which remains heretofore unresolved, as it requires us to observe directly in the inner parts at the AU scale. The Submillimeter Array (SMA)¹ (Ho et al. 2004), with the capability to probe warm and dense molecular gas at high angular resolution, can be and has been used to study the physical properties of the jets in detail (e.g., Hirano et al. 2006; Lee et al. 2007).

The HH 211 outflow is an archetypical outflow with a highly collimated jet, located in the IC 348 complex in Perseus. The distance of the IC 348 complex is assumed to be 320 pc (Lada et al. 2006), but it could be 250 pc (Enoch et al. 2006). The outflow was discovered in H₂ shock emission at 2.12 μm (McCaughrean et al. 1994), powered by a young, low-mass, and low-luminosity ($\sim 3.6 L_{\odot}$) Class 0 protostar with $T_{bol} < 33$ K (Froebrich 2005). A collimated CO jet was seen surrounded by cavity walls in CO ($J=2-1$) (Gueth & Guilloteau 1999, hereafter GG99). Recent observations with the SMA in SiO ($J=5-4$) (Hirano et al. 2006) and ($J=8-7$) (Palau et al. 2006) also revealed a collimated SiO jet consisting of a chain of spatially unresolved knots aligned with the CO jet, tracing shock emission along the jet. In this paper, we present observations of the jet in SiO ($J=8-7$) and CO ($J=3-2$) at higher-angular resolution than in Palau et al. (2006), in order to better constrain the physical properties and thus the launching mechanisms of the jet.

2. Observations

Observations toward the HH 211 jet were carried out with the SMA on 2004 October 4 and 18 in the compact configuration and on 2004 September 10 in the extended configuration. Note that the observation on 2004 October 18 was only a short partial track and thus not included in our analysis. The zenith opacities were $\tau_{230} \simeq 0.1$ and 0.13, respectively, on 2004 October 4 and 2004 September 10. SiO ($J = 8 - 7$) and CO ($J = 3 - 2$) lines were observed simultaneously with continuum using the 345 GHz band receivers. The receivers have two

¹ The Submillimeter Array is a joint project between the Smithsonian Astrophysical Observatory and the Academia Sinica Institute of Astronomy and Astrophysics, and is funded by the Smithsonian Institution and the Academia Sinica.

sidebands, lower and upper, covering the frequency range from 335.58 to 337.55 and from 345.59 to 347.56 GHz, respectively. Combining the line-free portions of the two sidebands results in a total continuum bandwidth of ~ 3.7 GHz centered at ~ 342 GHz (or $\lambda \sim 880 \mu\text{m}$) for the continuum. The baselines have projected lengths ranging from ~ 20 to 225 m. The primary beam has a size of $\sim 35''$ and three pointings were used to map the jet. For the correlator, 128 spectral channels were used for each 104 MHz chunk, resulting in a velocity resolution of $\sim 0.7 \text{ km s}^{-1}$ per channel.

The visibility data were calibrated with the MIR package, with Saturn, Venus, quasars 3C84 and J0355+508 as passband calibrators, quasars 3C84 and J0355+508 as gain calibrators, and Uranus ($\sim 70 \text{ Jy}$) as a flux calibrator. The flux uncertainty is estimated to be $\sim 20\%$. The calibrated visibility data were imaged with the MIRIAD package. The dirty maps that were produced from the calibrated visibility data were CLEANed using the Steer clean method, producing the CLEAN component maps. The final maps were obtained by restoring the CLEAN component maps with a synthesized (Gaussian) beam fitted to the main lobe of the dirty beam. With natural weighting, the synthesized beam has a size of $1''.28 \times 0''.84$ at a position angle (P.A.) of $\sim 70^\circ$. The rms noise level is $\sim 0.33 \text{ Jy beam}^{-1}$ in the channel maps and $6.5 \text{ mJy beam}^{-1}$ in the continuum map. The velocities of the channel maps are LSR. The typical rms of the gain phases is $\sim 20^\circ$, resulting in an absolute positional accuracy of one tenth of the synthesized beam, or $\sim 0''.1$.

3. Results

Our results are presented in comparison to the IR image (H_2 at $2.12 \mu\text{m}$ + continuum) made with the VLT on 2002 January 4 (Hirano et al. 2006), which shows clear shock interactions along the jet axis. Since our observations were carried out ~ 3 years later than the IR image, the H_2 shock knots and bow shocks might have moved down along the jet axis by $\sim 0''.2\text{--}0''.4$ from their positions in that image, assuming a typical jet velocity of $100\text{--}200 \text{ km s}^{-1}$. This movement, however, does not affect significantly our comparison and conclusions, considering that the angular resolution of our observations is $\sim 1''$ along the jet axis. The systemic velocity in this region is assumed to be 9.2 km s^{-1} LSR, as in Hirano et al. (2006) and Palau et al. (2006). Throughout this paper, the velocity is relative to this systemic value.

3.1. 342 GHz Continuum Emission

Continuum emission is detected at 342 GHz at the center of the H₂ flow with a total (integrated) flux of 0.44 ± 0.10 Jy. It has a peak at $\alpha_{(2000)} = 03^{\text{h}}43^{\text{m}}56^{\text{s}}.801$, $\delta_{(2000)} = 32^{\circ}00'50''.22$, with a positional uncertainty of $0''.1$ (Fig. 1). This peak position is within $0''.1$ of that found at 43.3 GHz (or $\lambda = 7$ mm) with the VLA at an angular resolution of $\sim 0''.15$ (Avila et al. 2001), and is thus considered as the position of the protostar throughout this paper. Note that the continuum flux here is about twice as that found in Palau et al. (2006), which was based on the observation on 2004 October 18. As mentioned, that observation was only a short partial track with poor uv coverage. Thus, even though their visibility amplitude versus uv distance plot is similar to ours, most of the extended emission was not recovered in their image (see their Fig. 1b).

The emission is seen extending $\sim 2''$ to the southwest from the protostar roughly perpendicular to the jet axis, similar to that seen at 230 GHz (GG99), likely tracing the flattened envelope perpendicular to the jet axis. The envelope, however, seems asymmetric with less emission extending to the northeast. Faint emission is also seen extending to the northwest, similar to that seen at 220 GHz (Hirano et al. 2006), probably tracing the envelope material around the west outflow lobe. Near the protostar, the structure is compact and not resolved, as seen in the map made using the visibility data with the uv distance greater than $100 \text{ k}\lambda$ (see Fig. 1b), with a flux of $\sim 0.08 \pm 0.02$ Jy. This unresolved compact source is also seen in the visibility amplitude versus uv distance plot, with a similar flux (Fig. 2a). The size (diameter) of this compact source has an upper limit of $\sim 0''.4$ or 130 AU set by the longest baseline. Two components, an envelope and a compact source, have also been suggested in other Class 0 sources, e.g., IRAS 16293-2422 and L1448-C (Schöier et al. 2004), and HH 212 (Codella et al. 2007; Lee et al. 2007).

The spectral energy distribution (SED) of the continuum source (see Fig. 2b) indicates that the continuum emission at 342 GHz is mainly thermal dust emission. Assuming a constant temperature T_d , a frequency-independent source size Ω , and a mass opacity $\kappa_\nu = 0.1(\nu/10^{12}\text{Hz})^\beta \text{ cm}^2 \text{ g}^{-1}$ (Beckwith et al. 1990) for the dust, the SED can be fitted with $T_d \sim 30 \text{ K}$, $\Omega \sim 3.6 \text{ arcsec}^2$, $\beta \sim 0.6$, and an optical depth $\tau_\nu \sim 0.086$ at 342 GHz. Our value of β is similar to that found by GG99 and Avila et al. (2001). The dust temperature is also consistent with the bolometric temperature, which was found to be $< 33 \text{ K}$ (Froebrich 2005). However, our β is smaller than that found including fluxes from the larger-scale envelope (with a mass of $\sim 0.8 M_\odot$) in photometric broadband observations, which is 1.3 (Froebrich 2005). $\beta > 1$ was also found toward large-scale envelopes around other embedded YSOs (Dent et al. 1998). Thus, excluding the larger-scale envelope tends to decrease the value of β , suggesting that the dust grains grow bigger toward the source. The compact source at

the center may have even lower β . To examine this, fluxes of the compact source at 342 and 220 GHz are compared with $F_\nu \propto \nu^2$ or $\beta = 0$. Assuming that fluxes at long baselines are dominated by the compact source, the fluxes are $\sim 0.08 \pm 0.02$ Jy at 342 GHz and 0.04 ± 0.02 Jy at 220 GHz (3 σ detection with the SMA data in Hirano et al. 2006, with 1 $\sigma \sim 0.013$ Jy beam $^{-1}$ and the uncertainty in flux scale ~ 20 %). The SED of the compact source at those frequencies seems roughly consistent with $\beta = 0$, or an optically thick emission, as in HH 212 (Codella et al. 2007). In addition, half of the emission at 43.3 GHz could be from the unresolved compact source. If the compact emission at 342 and 43.3 GHz are indeed arisen from the same region, then the compact source has a size (diameter) of $\lesssim 0''.1$ or 30 AU (Avila et al. 2001). Therefore, the compact source probably has different origin and is likely to be a warm (with a brightness temperature > 80 K) optically thick (accretion) disk deeply embedded in the cold envelope. Observations at higher angular resolution are really needed to confirm this.

The total mass of the continuum emission (including both the extended and compact components) is estimated to be $\sim 0.05 M_\odot$, assuming optically thin emission with a temperature of 30 K. Since part of the emission is likely to be optically thick, the mass here is only a lower limit.

3.2. SiO Jet

A knotty jet is seen in SiO, as in Palau et al. (2006), but with more knots resolved at higher angular resolution (Fig. 3c). It is bipolar with the blueshifted side in the southeast and the redshifted side in the northwest, but with the redshifted side brighter than the blueshifted side. It consists of a chain of knots on each side of the source with an interknot spacing of $\sim 2''-3''$ or 600–900 AU. It extends out to $\sim 18''$ away, with the innermost pair of knots at only $\sim 1''.7$ or 535 AU from the source. Most of the knots have H₂ counterparts, except for those in the inner part. The lack of H₂ counterparts there was already seen by Hirano et al. (2006) and attributed to the heavy dust extinction associated with the dense envelope as seen in H¹³CO⁺ (GG99) and NH₃ (Wiseman 2001).

3.3. Jet Axes

The eastern component and western component of the SiO jet are not exactly antiparallel (Fig. 3c). They are misaligned slightly by $\sim 1^\circ$, with their axes estimated to have a P.A. of $116.1^\circ \pm 0.5^\circ$ and $297.1^\circ \pm 0.5^\circ$, respectively, by connecting the source to the SiO knots.

Since their original paths of motion are likely to be antiparallel, this misalignment suggests a presence of a jet bending. Assuming both bent by the same degree, they are both bent by $\sim 0.5^\circ$ to the north with a jet (or mean) axis having a P.A. of $116.6^\circ \pm 0.5^\circ$. The peaks of the closest pair of the SiO knots (BK1 and RK1) are not exactly aligned with this jet axis, probably suggesting a slight precession of the jet. That the jet is slightly sinuous also supports this possibility. The angle of precession is estimated to be $< 1^\circ$.

The jet may also have a large-scale precession as discussed in GG99 and Eislöffel et al. (2003), with an angle of $\sim 3^\circ$. The axis of the SiO jet, which is aligned with the H₂ knots, is considered as the jet axis in the inner part out to H₂ bow shocks BB1 and RB1 (Fig. 3a). The jet axis in the outer part, which can be estimated by connecting the source to the tip of bow shock BB2 further out in the east, is found to be different by $\sim 3^\circ$ with a P.A. $\sim 113.6^\circ$ (indicated by the green dashed line). If we connect this axis to the west, the H₂ emission RB2 could be the counterpart of bow shock BB2 but mainly seen with the southern wing.

3.4. CO Jet and Shells

CO emission is detected not only along the jet axis but also toward outflow shells. In the following, two velocity ranges, high (from -23.7 to -8.7 km s⁻¹ and from 10.3 to 35.3 km s⁻¹) and low (from -5.7 to -1.7 km s⁻¹ and from 0.3 to 4.3 km s⁻¹, respectively for the blueshifted emission and redshifted emission), are selected to show these components.

A knotty jet-like structure is also seen in CO here at high velocity (Fig. 3d), as in lower excitation line (GG99). However, this jet-like structure actually contains two components, a jet component with a similar velocity structure to the SiO jet and a high-velocity shell component with a different velocity structure (see next section). With the selected velocity range, the high-velocity CO emission at $\sim 2''$ away from the source is mainly from the jet component. It is faint, associated with knots BK1 and RK1 seen in SiO, but slightly downstream.

At low velocity, rim-brightened shell-like structures are seen in CO (Fig. 4), coincident with those seen in the IR image, which are mainly from the continuum except near the bow shocks where the H₂ emission dominates (Eislöffel et al. 2003). These shell-like structures were also seen in lower excitation lines of CO and thought to trace the dense cavity walls of the outflow lobes produced by the H₂ bow shocks located at the ends of the jet (GG99). In the eastern lobe, however, the southern and northern shells are seen associated with two different bow shocks, BB1 and BB2, respectively. Thus, the shells likely trace the dense cavity walls recently shocked (excited) by the internal H₂ bow shocks at different jet axes

because of a large-scale jet precession (see §3.3).

3.5. Kinematics

Position-velocity (PV) diagrams of the SiO and CO emission cut along the jet axis are used to study the kinematics of the jet (Fig. 5). Note that the CO emission seen at low velocity (indicated by dashed lines) likely traces the cavity walls along the jet axis.

In the jet, the SiO emission is localized toward the knots, with a range of velocities detached from the systemic velocity: knots BK1, RK1, RK2, and RK5 are bright and seen with a velocity range of $\sim 25 \text{ km s}^{-1}$ (see also their spectra in Fig. 6), while other knots are faint and seen with a narrower velocity range. At high velocity, CO emission (labeled CO jet) also arises from the jet, showing a similar velocity structure with similar mean velocity but with narrower velocity range (see also Fig. 6). Thus, the SiO emission and the CO jet emission can be used together to study the kinematics of the jet. They are blueshifted in the east and redshifted in the west. They are, however, more redshifted (with a mean velocity of $\sim 20 \text{ km s}^{-1}$) in the west than blueshifted (with a mean velocity of $\sim -15 \text{ km s}^{-1}$) in the east. In addition, for each component of the jet, the velocity centroids of the individual knots are also different.

Linear velocity structures (indicated with solid lines) are seen in CO, as in lower excitation line (GG99), with the velocity magnitude increasing with the distance from the source. These velocity structures are different from that of the SiO jet. To study their origin, we plot in Figure 7 the emission of the linear velocity structure (marked by an ellipse) in the west, where it can be better separated from the jet emission. The emission is seen around the jet axis but brighter in the north, with the transverse width increasing with the distance from the source, surrounded by the rim-brightened IR shell (cavity wall). In the far end, the emission shows shell-like structures associated with the H_2 knots. In the near end, however, it is unclear but may show shell-like structures associated with the SiO knots (comparing Fig. 7 with Fig. 3c). PV cuts across the jet axis in the west at $11''$ and $12''$ in the far end, where the structure is better resolved, also show a ring-like velocity structure as expected for a shell (Fig. 8). Note that, in these PV cuts, the CO emission seen at low velocity is likely from the cavity wall. Therefore, the CO emission associated with the linear velocity structures likely traces the (internal) shells or wakes driven by the (internal) bow shocks (see, e.g., Raga & Cabrit 1993; GG99; Lee et al. 2001), surrounded by the dense cavity walls.

3.6. Temperature, Column Density, and Density

The CO emission is assumed to have an excitation temperature of 100 K in the jet and 50 K in the high-velocity shells. Note that, however, the CO emission, which was detected also in higher- J transitions in the far infrared, could have a higher excitation temperature (Giannini et al. 2001). The H_2 column density can be derived assuming a CO abundance of 8.5×10^{-5} (Frerking et al. 1982) and optically thin emission in local thermal equilibrium. It is found to be $(4 - 8) \times 10^{20} \text{ cm}^{-2}$ in the jet, which has an intensity of 57–104 K km s $^{-1}$ toward the knots (see Fig. 3d, integrated from -23.7 to -8.7 km s $^{-1}$ and 10.3 to 35.3 km s $^{-1}$), and $4.5 \times 10^{20} \text{ cm}^{-2}$ in the high-velocity shells, which have a mean intensity of 85 K km s $^{-1}$ (see Fig. 7, integrated from 0.3 to 20.3 km s $^{-1}$). The jet is unresolved with a size (diameter) of $< 1''$ and thus has a density of $> 10^5 \text{ cm}^{-3}$. Assuming a shell thickness of $\sim 1''$, the high-velocity shells have a density of $\sim 9 \times 10^4 \text{ cm}^{-3}$. Note that, however, it is not meaningful to derive the density for the low-velocity shells because their fluxes are mostly resolved out in our observations (see also GG99).

Using the $\text{SiO}(J = 5 - 4)$ observations from Hirano et al. (2006), the line ratio of $\text{SiO}(J = 8 - 7)/\text{SiO}(J = 5 - 4)$ is found to be ~ 0.7 for the first pair of knots but decreasing to ~ 0.4 at the far ends of the SiO jet (Fig. 9). Note that this line ratio has been found to be ~ 1.0 for the first pair of knots but decreasing to ~ 0.5 at the far ends of the SiO jet by Palau et al. (2006) at lower angular resolution. However, with their maps, we recalculated the line ratio at lower angular resolution using the same velocity interval and intensity cutoff level and found it to be ~ 0.8 for the first pair of knots, and thus consistent with ours within the flux uncertainty. The kinetic temperature of the SiO emission can be assumed to be 300 K for the first pair of knots but 100 K for the knots further out (Hirano et al. 2006). The density can be estimated by comparing the line ratio to that in the LVG calculations with an assumption of optically thin emission (Nisini et al. 2002). Note that, however, the emission could be optically thick (Cabrit et al. 2007). The density is estimated to be $\sim 4 \times 10^6 \text{ cm}^{-3}$ for the first pair of knots but decreasing to $\sim 3 \times 10^6 \text{ cm}^{-3}$ at the far ends of the SiO jet. These densities, however, are a factor of ~ 2 lower than those derived from the line ratio of $\text{SiO}(J = 5 - 4)/\text{SiO}(J = 1 - 0)$ in Hirano et al. (2006). A detailed study with multiple transitions of SiO will address this in a later paper (Hirano et al. in prep).

4. Molecular Jet

4.1. Shocks

The SiO knots are seen with a range of velocities, likely tracing the unresolved internal (bow) shocks (i.e., working surfaces) in the jet, as in HH 212 (Codella et al. 2007; Lee et al. 2007). It is thought that SiO abundance is greatly enhanced in the shocks as a consequence of grain sputtering or grain-grain collisions releasing Si-bearing material into the gas phase, which reacts rapidly with O-bearing species (e.g., O₂ and OH) to form SiO (Schilke et al. 1997; Caselli et al. 1997). The emission is consistent with its production in C-type shocks, with a velocity range of $\sim 25 \text{ km s}^{-1}$, similar to that found to produce the observed SiO column densities in molecular outflows (Schilke et al. 1997). At high velocity, CO is also seen tracing the shocks in the jet. It has smaller velocity range than SiO, tracing weaker shocks where the temperature and density are both lower. Observations at higher angular resolution are needed to study the morphological relationship between the CO and SiO emission by resolving their structures.

4.2. Inclination

The jet inclination, i , can be estimated from the mean velocity of the SiO emission, v_m , with $i = \sin^{-1}(v_m/v_j)$, where v_j is the jet velocity. The eastern and western components of the jet may have different inclinations because of their different mean velocities. Assuming a typical jet velocity of $100\text{--}200 \text{ km s}^{-1}$, the eastern and western components of the jet have an inclination of -8.6° to -4.3° and 11.4° to 5.7° , respectively. Note that, however, it is also possible that the eastern and western components of the jet have the same inclinations but different jet velocities as in T Tauri star jets (López-Martín et al. 2003).

4.3. Mass-loss rate

The mass-loss rate of the jet can be estimated from the CO emission of the knots. As mentioned, the knots likely trace the internal (bow) shocks or the jet itself but highly compressed by shocks. Since the knots are unresolved, the compression factor is assumed to be ~ 3 , as found in HH 212 at similar angular resolution (Lee et al. 2007). Note that, however, the actual compression factor due to the shocks could be higher, if the knots are resolved. Thus, the (two-sided) mass-loss rate is given by

$$\dot{M}_j \sim \frac{2}{3} v_j m_{\text{H}_2} N b \quad (1)$$

where N and b are the CO column density and the linear size of the synthesized beam perpendicular to the jet axis. With $N \sim (4 - 8) \times 10^{20} \text{ cm}^{-2}$ (see §3.6), $b \sim 5 \times 10^{15} \text{ cm}$, and $v_j \sim 100 - 200 \text{ km s}^{-1}$, $\dot{M}_j \sim (0.7 - 2.8) \times 10^{-6} M_\odot \text{ yr}^{-1}$, similar to that found in HH 212. The accretion rate can be estimated assuming that the bolometric luminosity L_{bol} is mainly from the accretion. Assuming a stellar mass of $M_* \sim 0.06 M_\odot$ (derived from an evolution model, Froebrich et al. 2003) and a stellar radius of $R_* \sim 4R_\odot$ (Stahler et al. 1980), then the accretion rate $\dot{M}_a \sim L_{\text{bol}}R_*/GM_* \sim 8 \times 10^{-6} M_\odot \text{ yr}^{-1}$, with $L_{\text{bol}} \sim 3.6L_\odot$ (Froebrich 2005). Thus, the mass-loss rate is estimated to be $\sim 9 - 36\%$ of the accretion rate, similar to that found in HH 212 (Lee et al. 2007).

4.4. Episodic, Bending, and Precessing

The jet is seen with a chain of knots in SiO and CO with a semiperiodic spacing of $\sim 2'' - 3''$ or 600–900 AU. The knots may trace the unresolved (bow) shocks resulting from a semiperiodic variation in the jet velocity (see, e.g., Suttner et al. 1997). A temporal variation in the jet properties was also suggested in GG99. The period, which can be estimated by dividing the interknot spacing by the jet velocity, is found to be $\sim 44 - 15 \text{ yr}$, assuming a jet velocity of 100–200 km s^{-1} . The jet is believed to be launched from an accretion disk around the source. The periodic velocity variation may be due to (1) periodic perturbation of the accretion disk by an unresolved companion at a few AU away or (2) magnetic cycle like the solar magnetic cycle, which has a period of $\sim 22 \text{ yr}$ (Shu et al. 1997).

The jet seems to have a small-scale ($< 1^\circ$) precession with a sinuous structure, in addition to a large-scale ($\sim 3^\circ$) precession suggested in GG99 and Eisloffel et al. (2003). Small-scale jet precession is also seen in other jets, e.g., HH 34 and HH 212, and is generally ascribed to the tidal effects of a companion star on the direction of the jet axis (Reipurth et al. 2002). However, it may also be due to kink instability in the jet (Todo et al. 1993).

The jet is also seen bent in SiO with its eastern and western components bent by $\sim 0.5^\circ$ to the north. The jet was also seen bent in CO but by 3 times larger (GG99) due to contamination from high-velocity shells (see §3.4 & §3.5). The jet may have an additional bending into the plane of the sky because the eastern and western components of the jet may have different inclinations due to their different mean velocities (see §4.2). Assuming their original paths of motion are antiparallel, the eastern and western components of the jet are both bent by $\sim 0.7^\circ - 1.4^\circ$ into the plane of the sky. Thus, the jet may have a total bending of $\sim 0.9^\circ - 1.5^\circ$. Possible mechanisms for jet bending have been discussed in Fendt & Zinnecker (1998) and GG99. One of the possibilities is due to motion of the jet source in a binary system. The envelope, which is seen elongated toward the southwest, may result from an

interaction with a companion in the southwest.

4.5. Rotating and Launching Radius?

The jet is expected to be rotating, carrying away extra angular momentum from accretion disk. The HH 211 jet, being close to the plane of the sky, is one of the best candidates to study the rotation. Here, only the first four bright SiO knots (BK1, BK3, RK1, and RK2) are used, because the SiO knots further out are likely to be more affected by shock interactions.

A velocity gradient is seen across the first four knots (see the solid lines in Fig. 10), with $\sim 1.5 \pm 0.8 \text{ km s}^{-1}$ at $\sim 30 \pm 15 \text{ AU}$ (i.e., $0''.1$) away from the jet axis. The jet may have a radius (i.e., jet edge) of $\sim 30 \text{ AU}$, similar to that of HH 212, which is estimated to be $\sim 45 \text{ AU}$ (Cabrit et al. 2007). However, the beam dilution due to insufficient angular resolution could make the velocity shift smaller than it really is (see, e.g., Pesenti et al. 2004). This velocity gradient has the same direction as that seen in the rotating ammonia envelope (Wiseman, private communication), suggesting that it is from the jet rotation. The velocity beyond $\pm 1.5 \text{ km s}^{-1}$ seems increasing toward the jet axis, also as predicted in magneto-centrifugal wind models.

However, the interpretation of the velocity gradient perpendicular to the jet axis is complicated by the presence of a velocity gradient along the jet axis (Fig. 11). On the blueshifted (east) side, the higher-blueshifted emission (blue contours) is upstream of the lower-blueshifted emission (red contours), while on the redshifted (west) side, the higher-redshifted emission (red contours) is upstream of the lower-redshifted emission (blue contours). This velocity gradient along the jet axis is consistent with the SiO knots being formed by a velocity variation in the jet (see §4.4), with the faster jet material catching up with the slower jet material. Without sufficient angular resolution, this velocity gradient can not be separated from the component perpendicular to the jet axis. The velocity gradient seen across the knots RK1 and BK1 may even arise from the velocity gradient along the jet axis due to the beam position angle. The jet also has a small-scale precession that may introduce a velocity asymmetry between the two jet edges (see Cerqueira et al. 2006). The increase in velocity toward the jet axis may also be due to the side-ways ejection of the shocked material. Therefore, further observations at higher angular resolution are really needed to confirm the jet rotation.

The launching radius of the jet can be estimated if the measured velocity gradient is indeed from the jet rotation. In magneto-centrifugal wind models, the jet can be considered

as the dense part of the wind along the rotational axis. In the wind, the specific angular momentum and energy can be assumed to be conserved along any given field line. Thus, for a given stellar mass, the specific angular momentum and poloidal velocity (i.e., jet velocity) at large distance can be used to derive the angular velocity and thus the wind launching radius at the foot point of the field line in the accretion disk (see, e.g., Anderson et al. 2003). The angular velocity at the foot point is found to be $\Omega_0 \sim (0.82 - 3.23) \times 10^{-6} \text{ s}^{-1}$ or $0.07\text{--}0.28 \text{ day}^{-1}$, using Eq. 4 in Anderson et al. (2003), assuming a stellar mass of $M_* \sim 0.06 M_\odot$ (Froebich et al. 2003) and a jet velocity of $100\text{--}200 \text{ km s}^{-1}$. Thus, the wind launching radius is $\bar{\omega}_0 \sim 0.15 - 0.06 \text{ AU}$ or $\sim (8 - 3)R_*$, with the stellar radius $R_* \sim 4R_\odot$ (Stahler et al. 1980). Therefore, the jet could be launched either from near the corotation radius ($\sim 0.05 \text{ AU}$) as in the X-wind model (Shu et al. 2000) or beyond in the inner edge ($\sim 0.1 \text{ AU}$) of a disk as in disk-wind model (Konigl & Pudritz 2000), depending on the jet velocity. Note that, if the jet is really launched from near the corotation radius, the rotation period of the protostar would be locked to be ~ 22 days. A classical T Tauri star has been found to have a typical rotation period of ~ 8 days (see, e.g., Bouvier et al. 1993), with a stellar mass of $0.5\text{--}0.8 M_\odot$. The protostar here in HH 211, with a mass of ~ 10 times smaller, could have a rotation period of ~ 3 times longer.

5. Conclusions

We have mapped the protostellar jet HH 211 in 342 GHz continuum, SiO ($J = 8 - 7$), and CO ($J = 3 - 2$) emission. Thermal dust emission is seen in continuum at the center of the jet, tracing an envelope and a possible optically thick compact disk (with a size $< 130 \text{ AU}$) around the protostar. A knotty jet is seen in CO and SiO as in H₂, but extending closer to the protostar. It consists of a chain of knots on each side of the protostar, with an interknot spacing of $\sim 2''\text{--}3''$ or $600\text{--}900 \text{ AU}$ and the innermost pair of knots at only $\sim 1''.7$ or 535 AU from the protostar. These knots likely trace unresolved internal (bow) shocks in the jet, with a velocity range up to $\sim 25 \text{ km s}^{-1}$. The jet is episodic, precessing, and bending. The two-sided mass-loss rate of the jet is estimated to be $\sim (0.7 - 2.4) \times 10^{-6} M_\odot \text{ yr}^{-1}$, about $9\text{--}36\%$ of the accretion rate. A velocity gradient is seen consistently across two bright SiO knots (BK3 and RK2) perpendicular to the jet axis, with $\sim 1.5 \pm 0.8 \text{ km s}^{-1}$ at $\sim 30 \pm 15 \text{ AU}$, suggesting a presence of a jet rotation. The launching radius of the jet, derived from the potential jet rotation, is $\sim 0.15\text{--}0.062 \text{ AU}$ in the inner disk.

We thank the SMA staff for their efforts in running and maintaining the array, and the anonymous referee for the insightful comments. C.-F. Lee thanks Frank H. Shu, Zhi-Yun Lee, and Nagayoshi Ohashi for fruitful conversations. A. P. is grateful to Robert Estalella

for helpful discussions.

REFERENCES

- Anderson, J. M., Li, Z.-Y., Krasnopolsky, R., & Blandford, R. D. 2003, *ApJ*, 590, L107
- Avila, R., Rodríguez, L. F., & Curiel, S. 2001, *Revista Mexicana de Astronomía y Astrofísica*, 37, 201
- Beckwith, S. V. W., Sargent, A. I., Chini, R. S., & Guesten, R. 1990, *AJ*, 99, 924
- Bouvier, J., Cabrit, S., Fernandez, M., Martin, E. L., & Matthews, J. M. 1993, *A&A*, 272, 176
- Cabrit, S., Codella, C., Gueth, F., Nisini, B., Gusdorf, A., Dougados, C., & Bacciotti, F. 2007, *A&A*, in press
- Caselli, P., Hartquist, T. W., & Havnes, O. 1997, *A&A*, 322, 296
- Cerqueira, A. H., Velázquez, P. F., Raga, A. C., Vasconcelos, M. J., & de Colle, F. 2006, *A&A*, 448, 231
- Codella, C., Cabrit, S., Gueth, F., Cesaroni, R., Bacciotti, F., Lefloch, B., & McCaughrean, M. J. 2007, *A&A*, 462, L53
- Dent, W. R. F., Matthews, H. E., & Ward-Thompson, D. 1998, *MNRAS*, 301, 1049
- Eisloffel, J., Froebrich, D., Stanke, T., & McCaughrean, M. J. 2003, *ApJ*, 595, 259
- Enoch, M. L., et al. 2006, *ApJ*, 638, 293
- Fendt, C., & Zinnecker, H. 1998, *A&A*, 334, 750
- Frerking, M. A., Langer, W. D., & Wilson, R. W. 1982, *ApJ*, 262, 590
- Froebrich, D. 2005, *ApJS*, 156, 169
- Froebrich, D., Smith, M. D., Hodapp, K.-W., & Eisloffel, J. 2003, *MNRAS*, 346, 163
- Giannini, T., Nisini, B., & Lorenzetti, D. 2001, *ApJ*, 555, 40
- Gueth, F. & Guilloteau, S. 1999, *A&A*, 343, 571

- Hirano, N., Liu, S.-Y., Shang, H., Ho, P. T. P., Huang, H.-C., Kuan, Y.-J., McCaughrean, M. J., & Zhang, Q. 2006, *ApJ*, 636, L141
- Ho, P. T. P., Moran, J. M., & Lo, K. Y. 2004, *ApJ*, 616, L1
- Konigl, A., & Pudritz, R. E. 2000, *Protostars and Planets IV*, 759
- Lada, C. J., et al. 2006, *AJ*, 131, 1574
- Lee, C.-F., Stone, J. M., Ostriker, E. C., & Mundy, L. G. 2001, *ApJ*, 557, 429
- Lee, C.-F., Ho, P. T. P., Hirano, N., Beuther, H., Bourke, T. L., Zhang, Q., & Shang, H. 2007, *ApJ*, 659, 499
- López-Martín, L., Cabrit, S., & Dougados, C. 2003, *A&A*, 405, L1
- McCaughrean, M. J., Rayner, J. T., & Zinnecker, H. 1994, *ApJ*, 436, L189
- Nisini, B., Codella, C., Giannini, T., & Richer, J. S. 2002, *A&A*, 395, L25
- Palau, A., Ho, P. T. P., Zhang, Q., Estalella, R., Hirano, N., Shang, H., Lee, C.-F., Bourke, T. L., Beuther, H., & Kuan, Y.-J. 2006, *ApJ*, 636, L137
- Pesenti, N., Dougados, C., Cabrit, S., Ferreira, J., Casse, F., Garcia, P., & O'Brien, D. 2004, *A&A*, 416, L9
- Pudritz, R. E., Ouyed, R., Fendt, C., & Brandenburg, A. 2007, *Protostars and Planets V*, 277
- Raga, A. & Cabrit, S. 1993, *A&A*, 278, 267
- Ray, T., Dougados, C., Bacciotti, F., Eislöffel, J., & Chrysostomou, A. 2007, *Protostars and Planets V*, 231
- Rebull, L. M., et al. 2007, *ArXiv Astrophysics e-prints*, arXiv:astro-ph/0701711
- Reipurth, B., Heathcote, S., Morse, J., Hartigan, P., & Bally, J. 2002, *AJ*, 123, 362
- Schilke, P., Walmsley, C. M., Pineau des Forets, G., & Flower, D. R. 1997, *A&A*, 321, 293
- Schöier, F. L., Jørgensen, J. K., van Dishoeck, E. F., & Blake, G. A. 2004, *A&A*, 418, 185
- Shang, H., Li, Z.-Y., & Hirano, N. 2007, *Protostars and Planets V*, 261
- Shu, F. H., Shang, H., Glassgold, A. E., & Lee, T. 1997, *Science*, 277, 1475

Shu, F.H., Najita, J., Shang, H., & Li, Z. -Y. 2000, in Protostars and Planets IV, ed. V. Mannings, A. P. Boss & S. S. Russell (Tucson: University of Arizona Press), 789

Stahler, S. W., Shu, F. H., & Taam, R. E. 1980, ApJ, 241, 637

Suttner, G., Smith, M. D., Yorke, H. W. & Zinnecker, H. 1997, A&A, 318, 595

Todo, Y., Uchida, Y., Sato, T., & Rosner, R. 1993, ApJ, 403, 164

Wiseman, J. 2001, Science with the Atacama Large Millimeter Array, 235, 179

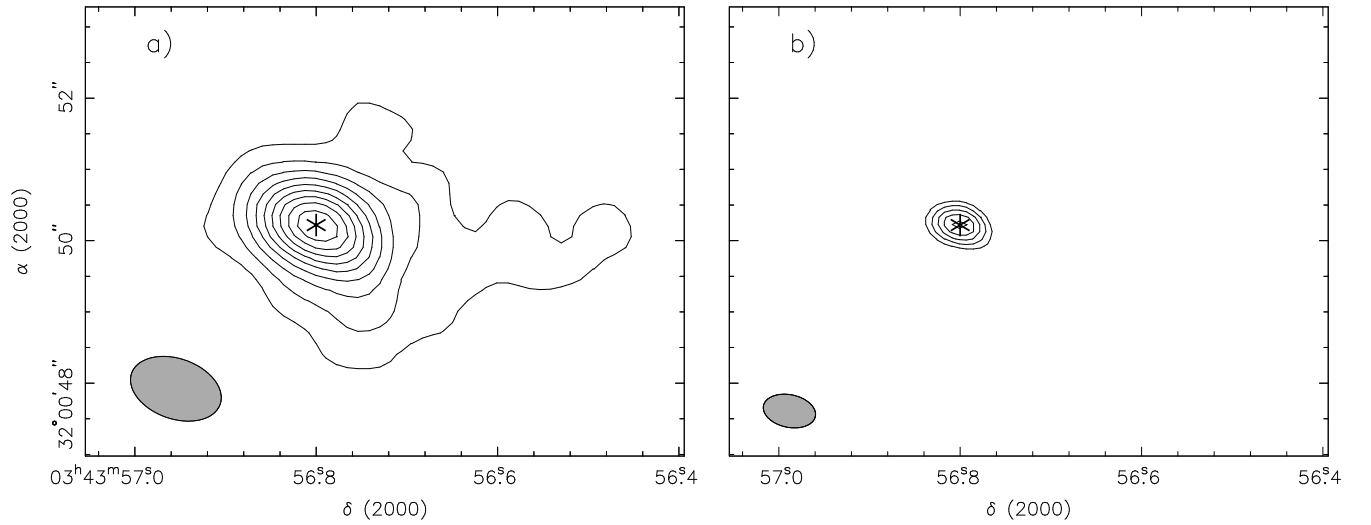


Fig. 1.— 342 GHz continuum maps with the asterisk marking the source position. (a) Map made using all the available visibility data. The contours go from 10 to 90% of the peak value, which is 155 mJy beam⁻¹. The beam is 1''.28 × 0''.84 with a P.A. of ~ 70°. (b) Map made using the visibility data with the *uv* distance greater than 100 kλ, showing the central compact source. The contours go from 35 to 95% with a step of 15% of the peak value, which is 77 mJy beam⁻¹. The beam is 0''.74 × 0''.46 with a P.A. of ~ 78°.

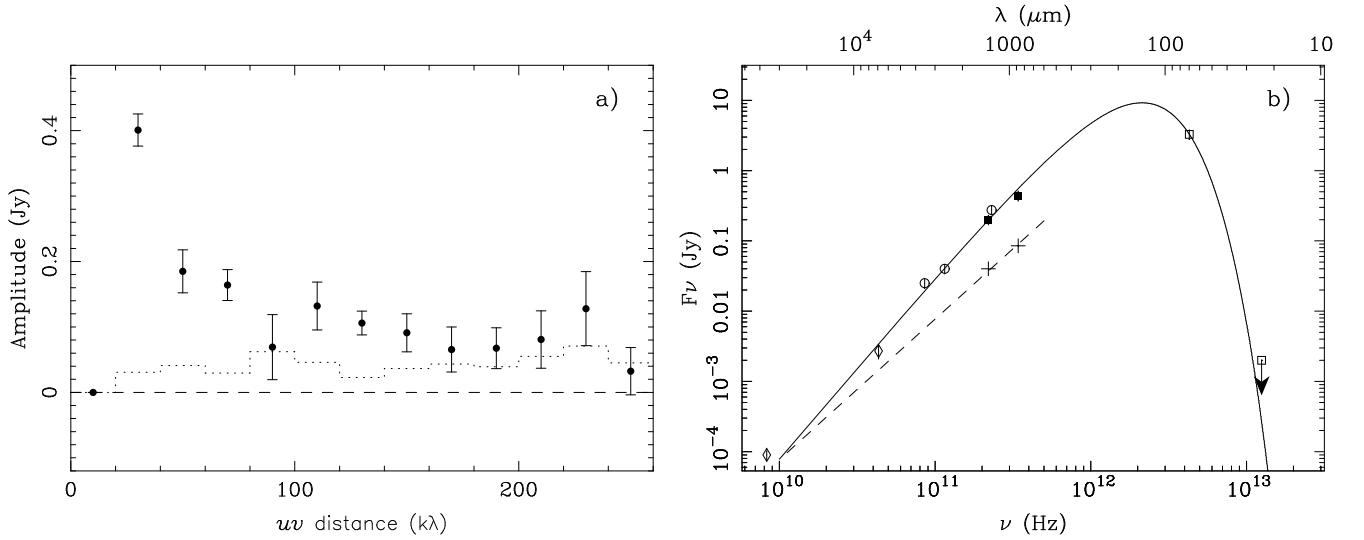


Fig. 2.— (a) Visibility amplitude versus uv distance plot for the continuum source with 1σ error bars. The dotted histogram is the zero-expectation level ($\sim 1.25\sigma$). (b) Spectral energy distribution (SED) of the continuum source. The filled squares are from our SMA observations. The open squares, open circles, and diamonds are from the Spitzer [$70\ \mu\text{m}$ from Rebull et al. (2007) and $24\ \mu\text{m}$ from Karl Stapelfeldt, private communication], PdBI (GG99), and VLA (Avila et al. 2001) observations, respectively. The crosses indicate the fluxes from the central unresolved point source estimated from our SMA observations at 342 and 220 GHz. The solid line shows the single-temperature fit to the SED of the continuum source (see text for detail). The dashed line shows the relation $F_\nu \propto \nu^2$ for the central compact source.

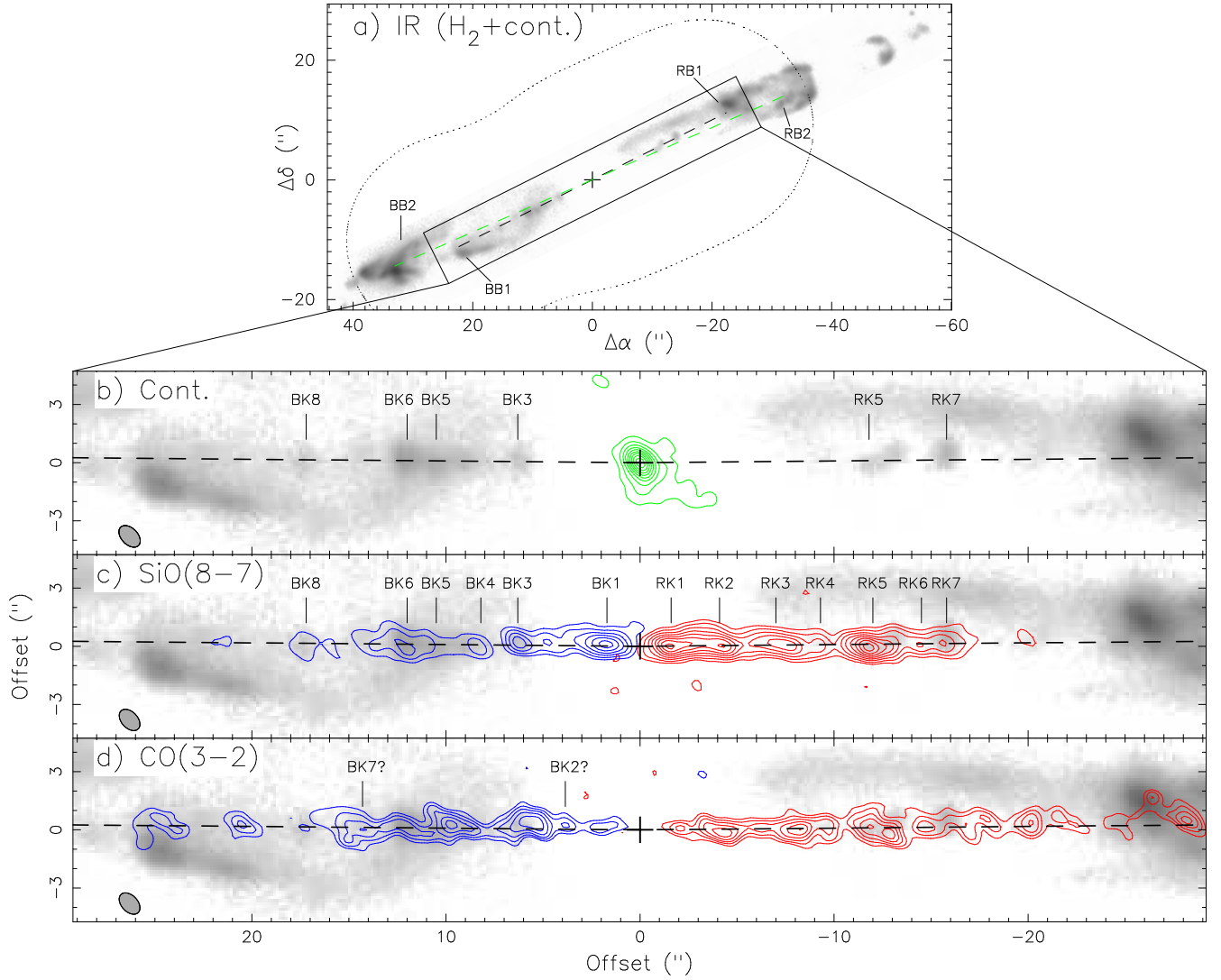


Fig. 3.— (a) The IR image adopted from Hirano et al. (2006). The dotted line outlines our observed region. The dashed lines indicate the jet axes. The cross marks the source position. Here BBx and RBx indicate blueshifted and redshifted bow shocks, respectively. (b) 342 GHz continuum contours (as in Fig. 1a) on top of the IR image. (c) Redshifted (6 to 34 km s⁻¹) and blueshifted (-22 to -2 km s⁻¹) SiO contours on top of the IR image. Contour spacing is 4 Jy beam⁻¹ km s⁻¹ (37.8 K km s⁻¹) with the first contour at 4 Jy beam⁻¹ km s⁻¹. Here, knots RK1, RK3, RK5, RK7, BK1, BK3, BK5, BK6, and BK8 correspond to knots R1, R2, R3, R4, B1, B2, B3, B4, and B5, respectively, in Hirano et al. (2006). Here BKx and RKx indicate blueshifted and redshifted knots, respectively. (d) High-velocity redshifted (10.3 to 35.3 km s⁻¹) and blueshifted (-23.7 to -8.7 km s⁻¹) CO contours on top of the IR image. Contour spacing is 1.5 Jy beam⁻¹ km s⁻¹ (14.2 K km s⁻¹) with the first contour at 3 Jy beam⁻¹ km s⁻¹ (28.4 K km s⁻¹). In (b), (c), and (d), the beams are 1".28×0".84 and the images are rotated by 26.6° clockwise. The western and eastern components of the jet axis are seen bent by ~ 0.5° to the north.

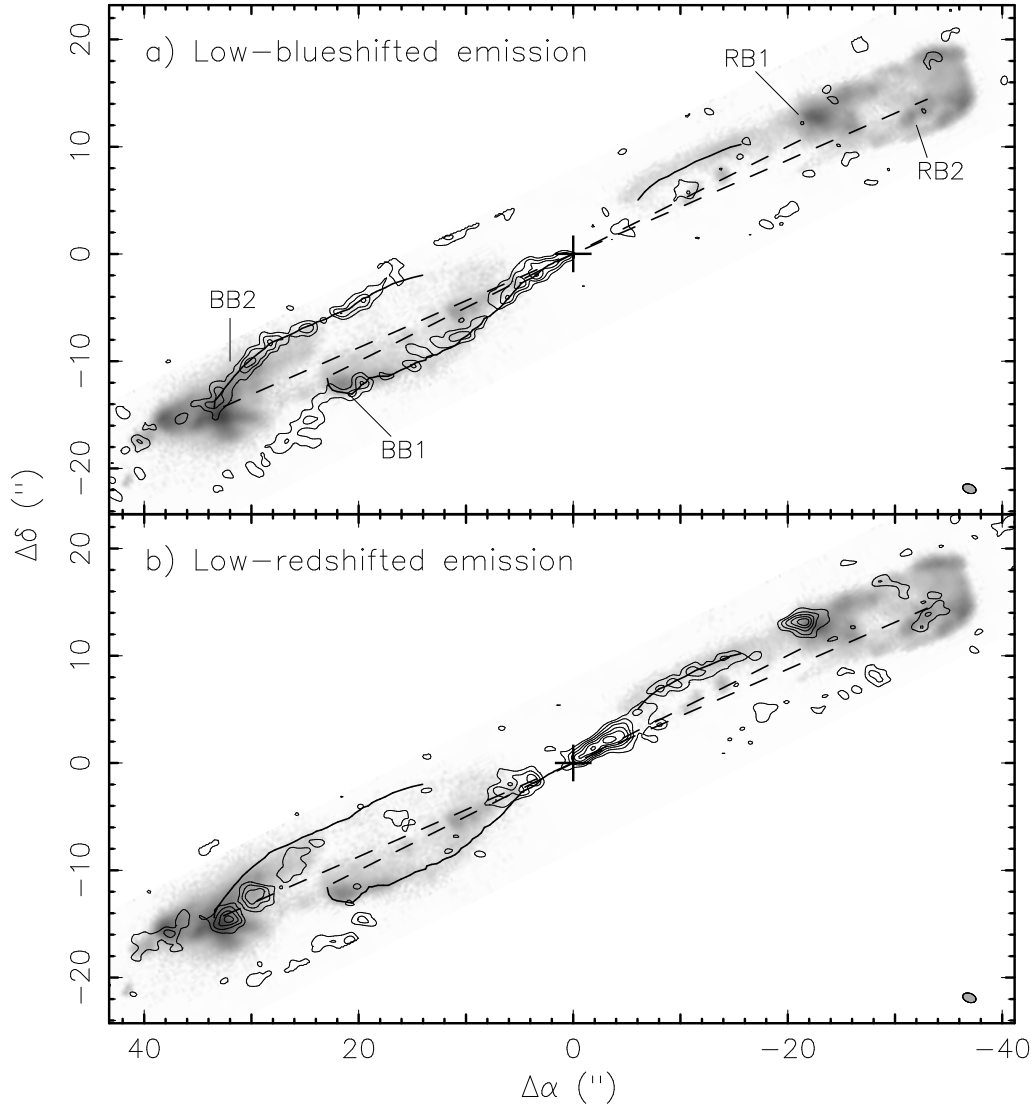


Fig. 4.— Low-velocity CO contours on top of the IR image. The beams are $1''.28 \times 0''.84$. The cross marks the source position. (a) shows the low-redshifted CO emission integrated from 0.3 to 4.3 km s^{-1} . (b) shows the low-blueshifted CO emission integrated from -5.7 to -1.7 km s^{-1} . Contour spacing is $1.4 \text{ Jy beam}^{-1} \text{ km s}^{-1}$ with the first contour at $1.4 \text{ Jy beam}^{-1} \text{ km s}^{-1}$.

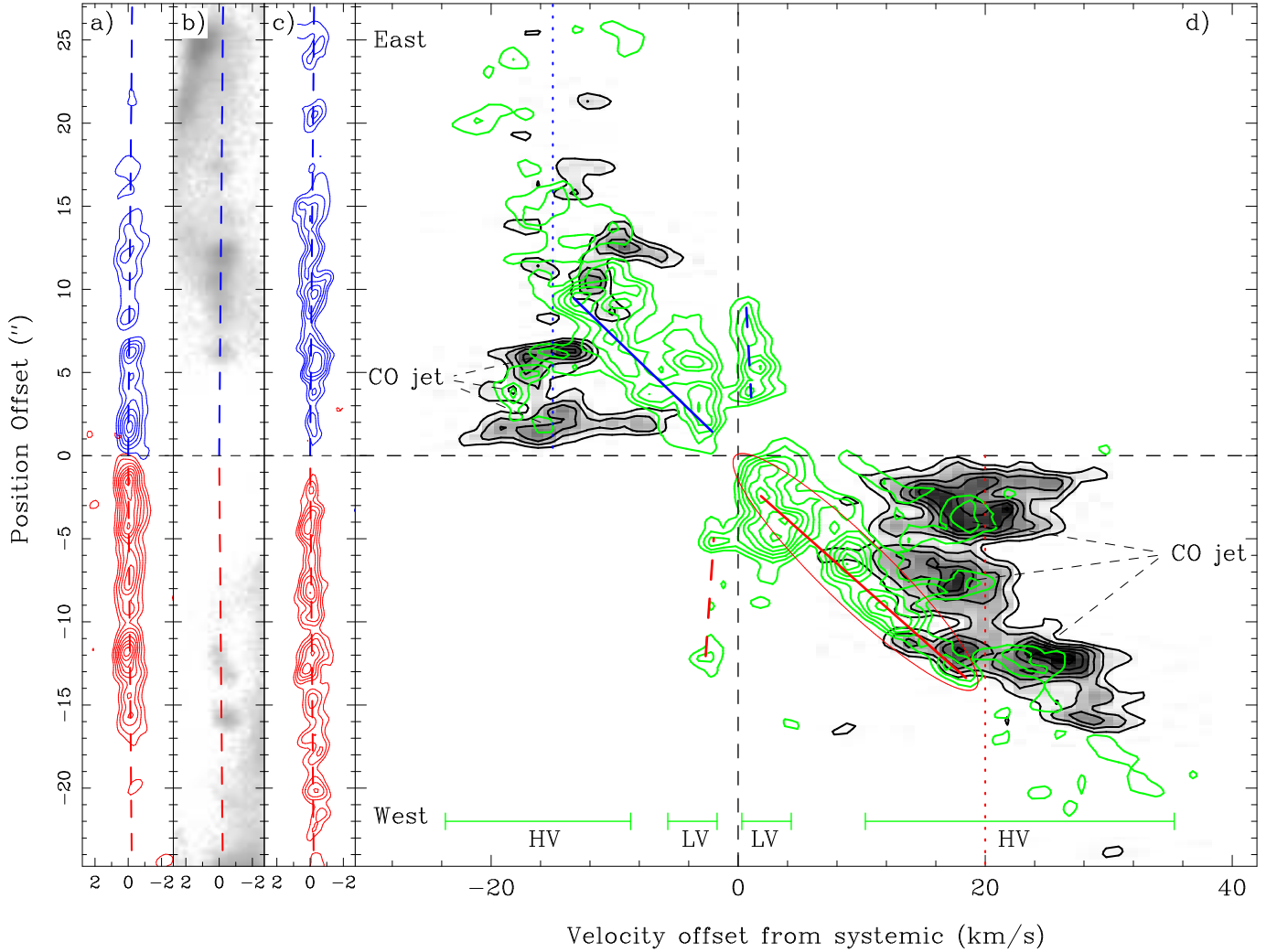


Fig. 5.— PV diagrams of the SiO and CO emission cut along the jet axis with a width of $1''$. (a) SiO contours, (b) IR image, and (c) high-velocity CO contours, as in Fig. 3. (d) PV diagrams of the SiO (black contours with image) and CO (green contours) emission. The SiO contours have a spacing of $0.25 \text{ Jy beam}^{-1}$ (2.36 K) with the first contour at 0.5 Jy beam^{-1} (4.73 K). The CO contours have a spacing of $0.225 \text{ Jy beam}^{-1}$ (2.12 K) with the first contour at $0.45 \text{ Jy beam}^{-1}$ (4.25 K). The red and blue dashed lines mark the emission from the low-velocity shells. The red and blue solid lines mark the emission from the high-velocity shells. The ellipse outlines the emission from the high-velocity shell in the west. The red and blue dotted lines indicate the mean velocities of the jet on the redshifted and blueshifted sides, respectively. Here, HV and LV denote the high-velocity and low-velocity ranges, respectively, for the CO emission.

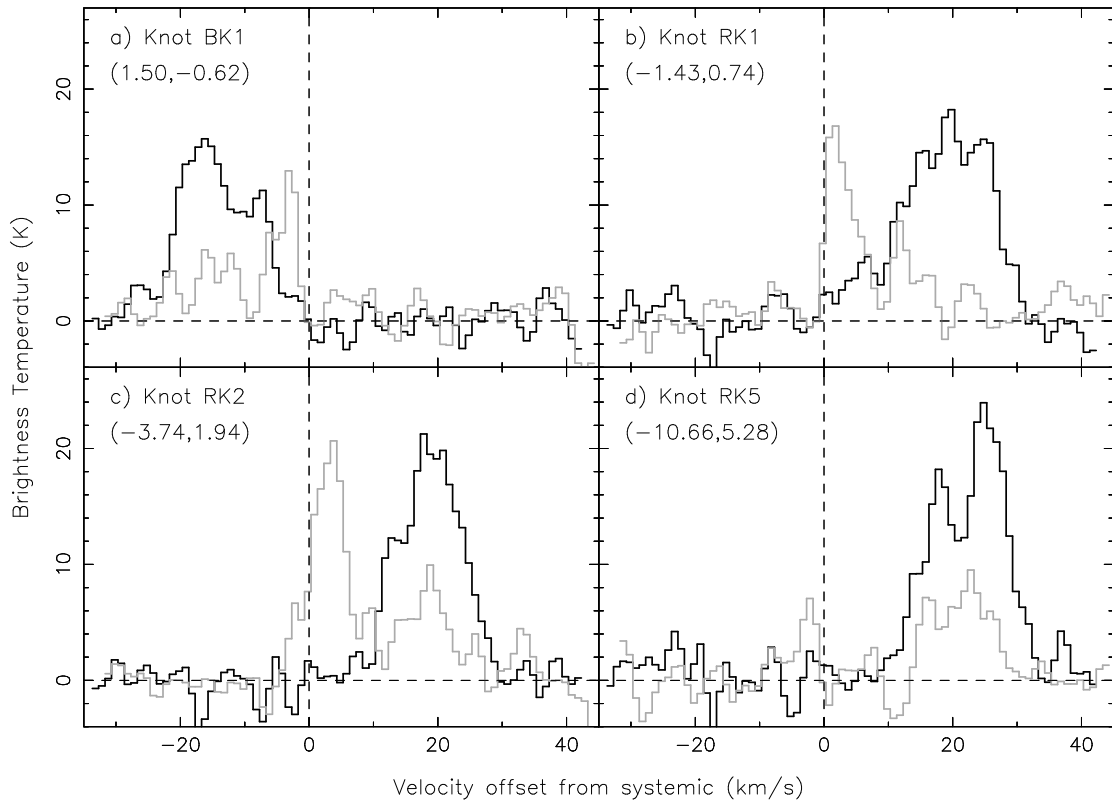


Fig. 6.— SiO (dark) and CO (gray) spectra toward four bright knots with their positions given in the upper left corners.

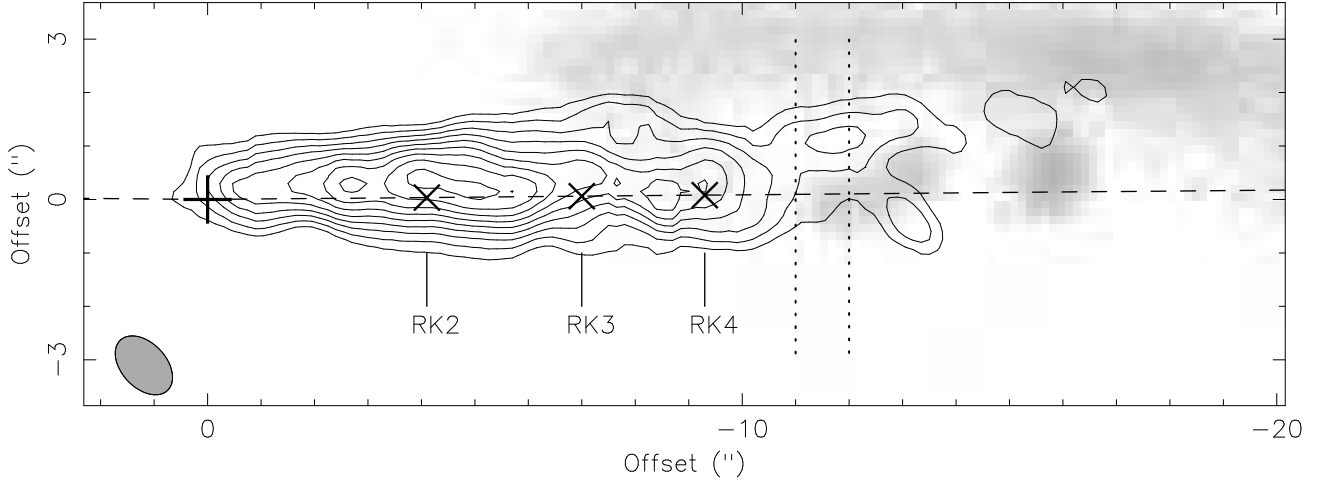


Fig. 7.— CO emission (0.3 to 20.3 km s^{-1}) associated with the linear velocity structure in the west, which is marked with an ellipse in Figure 5, plotted on top of the IR image. The image is rotated by 26.6° clockwise. Contour spacing is $1.4 \text{ Jy beam}^{-1} \text{ km s}^{-1}$ ($13.24 \text{ K km s}^{-1}$) with the first contour at $1.4 \text{ Jy beam}^{-1} \text{ km s}^{-1}$. The cross marks the source position. The Xs mark the positions of three SiO knots. The dashed line indicates the jet axis. The dotted lines indicate the locations of the PV cuts shown in Figure 8.

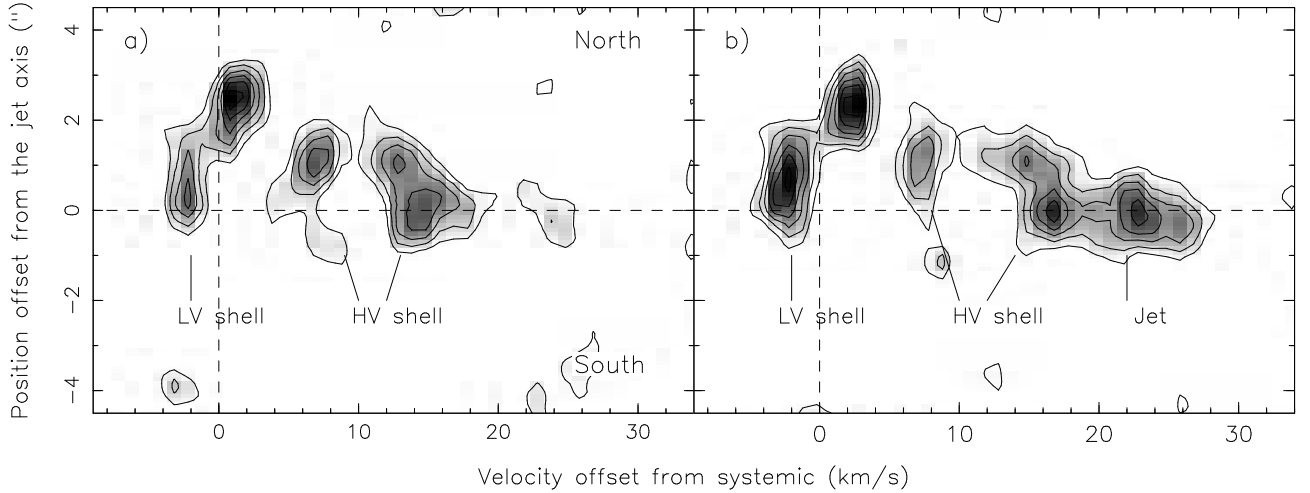


Fig. 8.— CO PV cuts perpendicular to the jet axis in the redshifted lobe at (a) $11''$ and (b) $12''$ away from the source. The cuts have a width of $1''$. Contour spacing is $0.15 \text{ Jy beam}^{-1}$ (1.42 K) with the first contour at 0.2 Jy beam^{-1} (1.89 K). Here LV and HV shells mean the low-velocity and high-velocity shells, respectively.

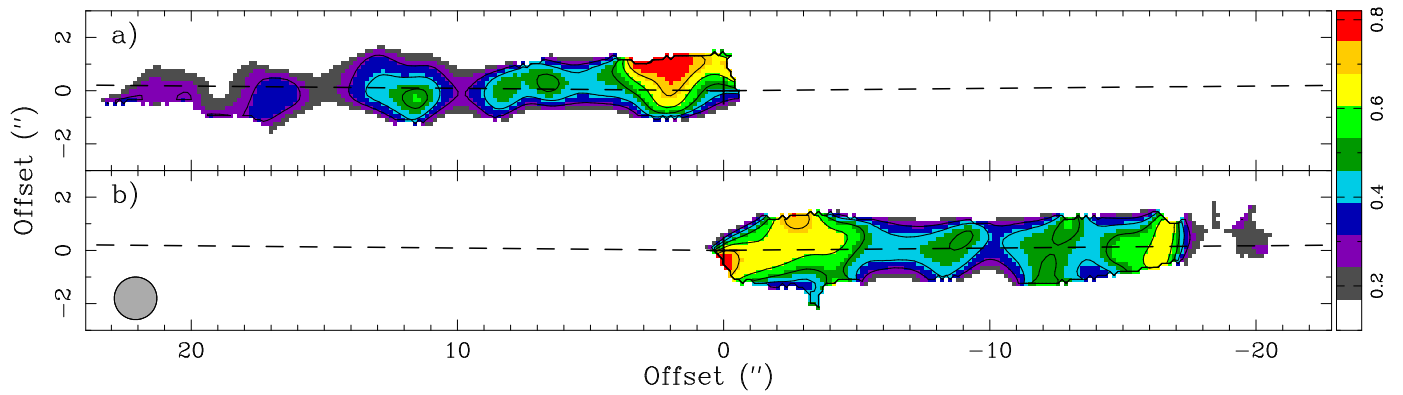


Fig. 9.— Maps of $\text{SiO}(J = 8 - 7)/\text{SiO}(J = 5 - 4)$ ratio, obtained from the (integrated) $\text{SiO}(J = 8 - 7)$ and $\text{SiO}(J = 5 - 4)$ maps that have been smoothed to the same angular resolution of $1''.6$. (a) Blueshifted side, with the emission integrated from -22 to -2 km s^{-1} . (b) Redshifted side, with the emission integrated from 6 to 34 km s^{-1} . Contour spacing is 0.1 with the first contour at 0.3 .

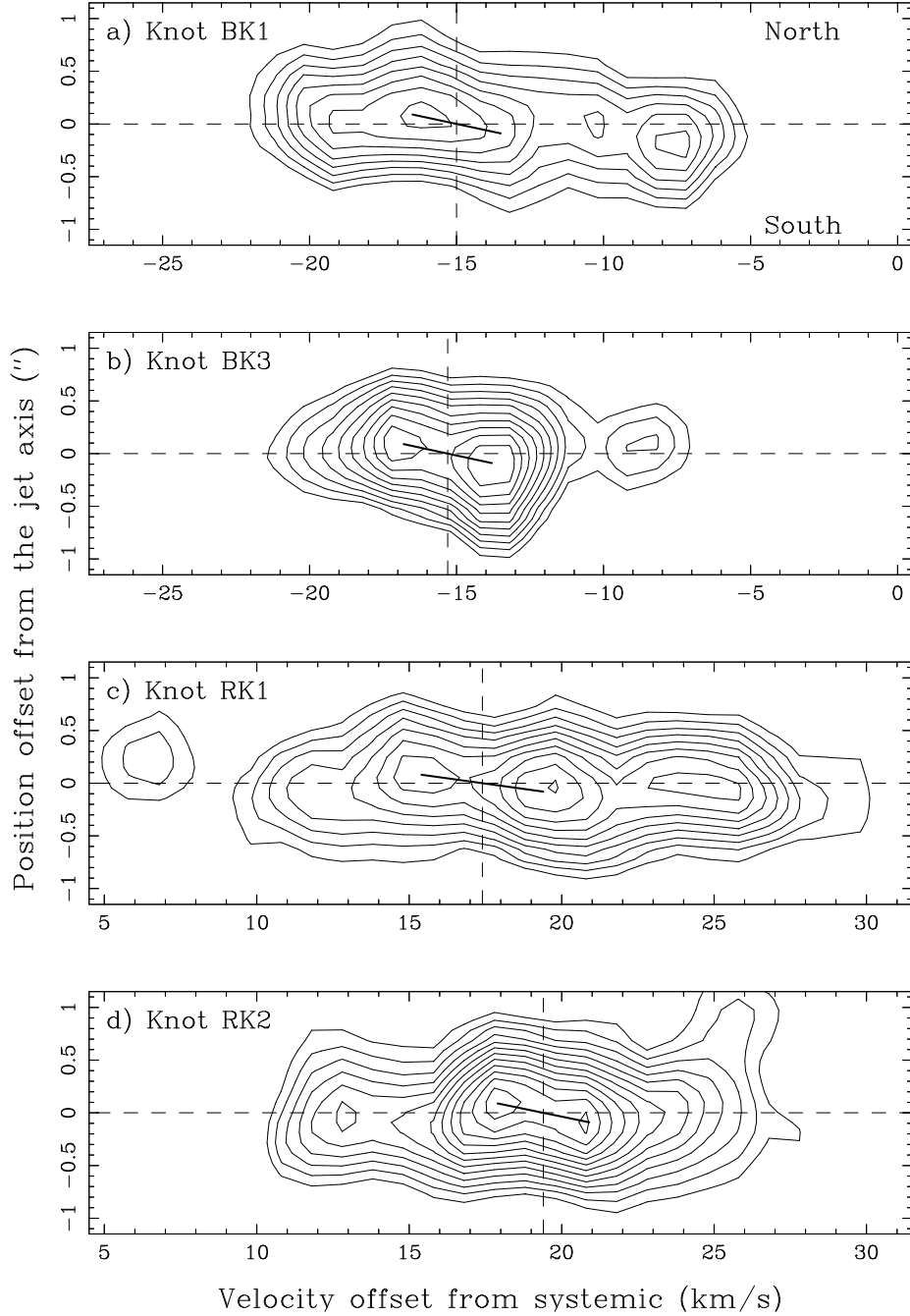


Fig. 10.— PV diagrams of the SiO emission cut perpendicular to the jet axis across the emission peaks of knots (a) BK1, (b) BK3, (c) RK1, and (d) RK2. The cuts have a width of $0''.3$. The solid lines define the velocity gradients across the jet axis by connecting the two peaks on the opposite sides. Contour spacing is $0.15 \text{ Jy beam}^{-1}$ (1.42 K) with the first contour at $0.45 \text{ Jy beam}^{-1}$ (4.25 K).

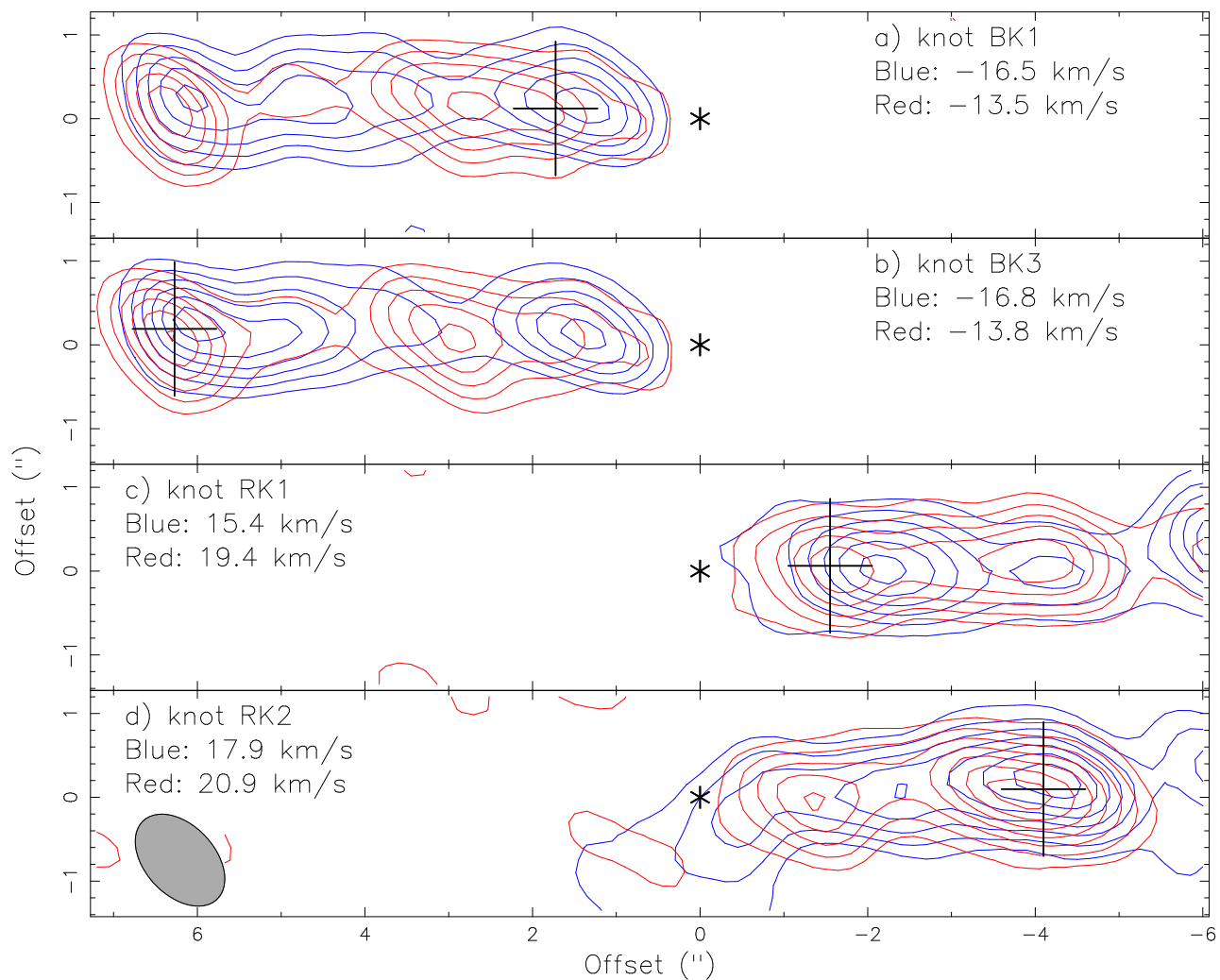


Fig. 11.— 1 km s^{-1} wide maps of the two line peaks that define their velocity gradient shown in Figure 10 for knots (a) BK1, (b) BK3, (c) RK1, and (d) RK2. Contour spacing is $0.45 \text{ Jy beam}^{-1}$ (4.25 K) with the first contour at $0.30 \text{ Jy beam}^{-1}$ (2.83 K). The crosses mark the cut centers where the emission peaks are in the integrated maps (see Fig. 3c). The asterisks mark the source position.